

This is the accepted manuscript made available via CHORUS. The article has been published as:

Glass Transition by Gelation in a Phase Separating Binary Alloy

R. E. Baumer and M. J. Demkowicz

Phys. Rev. Lett. **110**, 145502 — Published 2 April 2013

DOI: [10.1103/PhysRevLett.110.145502](https://doi.org/10.1103/PhysRevLett.110.145502)

1 Glass Transition by Gelation in a Phase Separating Binary Alloy

2
3 R. E. Baumer[†] and M. J. Demkowicz

4
5 Department of Materials Science and Engineering
6 Massachusetts Institute of Technology, Cambridge, MA 02139, USA

7 (Dated: January 14, 2013)

8 [†]rebaumer@mit.edu

9
10 ***Abstract***

11 We use molecular dynamics simulations to show that glass transition in a model phase separating
12 alloy, Cu₅₀Nb₅₀, occurs by gelation. At the glass transition, a mechanically stiff, percolating
13 network of atoms with icosahedral local packing forms at the interfaces between compositionally
14 enriched regions. This low-energy network halts coarsening of the phase-separated structure and
15 imparts shear resistance. These features of glass transition are remarkably similar to gelation
16 processes in polymeric and colloidal gels.

The existence of amorphous metals in alloy systems with positive heats of mixing ($\Delta H_{\text{MIX}} > 0$) is surprising in the face of traditional metallic glass design guidelines, which identify compositions near deep eutectics with negative heats of mixing as the best glass formers [1, 2]. While phase separating binary systems such as Cu-Nb [3] or Ni-Ag [4] are admittedly poor glass formers, calorimetry shows that sputter deposited amorphous metals with these compositions exhibit a lower than expected crystallization enthalpy ($\sim 10 \text{ kJ mol}^{-1}$) [3], suggesting that some form of atomic ordering stabilizes these amorphous solids [5]. Experiments [3] and simulations [4] indeed show that these alloys contain “spinodal-like” patterns of nanometer-scale compositional enrichment as well as percolating networks of local icosahedral atom packing [6]. However, the relationship between icosahedral short-range order (ISRO), compositional medium-range order (CMRO), and glass transition has not been determined.

Using molecular dynamics (MD) simulations in a model phase separating amorphous metal alloy— $\text{Cu}_{50}\text{Nb}_{50}$ —we show that a percolating network of ISRO forms at interfaces between compositionally enriched regions and leads to glass transition. Below the glass transition temperature T_G , the ISRO network is mechanically stiff, imparts shear resistance, and halts coarsening of the CMRO. The ISRO network constrains the dynamics of surrounding atoms and leads to anomalous diffusion. This ISRO network and its influence on the physical properties of the system bears striking resemblance to gelation in colloidal systems, in which a system-spanning, dynamically arrested network of locally preferred structures imparts stiffness [7, 8]. We discuss the potential technological implications of these findings for the synthesis of more conventional metallic glasses.

We select $\text{Cu}_{50}\text{Nb}_{50}$ as a model phase separating amorphous metal alloy because the CMRO of this system is well characterized via atom-probe tomography (APT) [3]. We model $\text{Cu}_{50}\text{Nb}_{50}$ using our previously developed embedded atom method (EAM) potential [9] and the open-source code LAMMPS [10]. The potential predicts a liquid-phase miscibility gap between 25-75% Cu [11]. Equilibrium liquid atomic structures of $\text{Cu}_{50}\text{Nb}_{50}$ are obtained by melting a 48,778 atom $\text{Cu}_{50}\text{Nb}_{50}$ system above the miscibility gap via a 1 ns anneal at zero pressure and 4000 K in the NPT Nosé-Hoover ensemble. The liquid $\text{Cu}_{50}\text{Nb}_{50}$ is rapidly quenched with zero applied pressure at 10^{13} K s^{-1} using stepwise cooling in 25 K decrements to 300 K (simulation

cell size $L_0 = 9.2$ nm at 300 K), with a velocity rescaling thermostat and Nosé-Hoover NPH barostat [12]. Structures quenched to different temperatures are annealed for 20 ns to investigate their thermal stability, while smaller systems (9,826 atoms) were annealed for up to 100 ns to quantify diffusion properties. All equations of motion are integrated with a timestep of 2 fs under periodic boundary conditions in cubic simulation cells. Radial distribution functions confirm that as-quenched and annealed $\text{Cu}_{50}\text{Nb}_{50}$ structures are fully amorphous. The temperature dependence of volume and enthalpy shows no evidence of a first order phase transition. Composition modulations in as-quenched structures are consistent with APT results on $\text{Cu}_{55}\text{Nb}_{45}$ [3], confirming that our MD modeling yields amorphous structures representative of vapor-deposited Cu-Nb amorphous films [Fig. S1].

The $\text{Cu}_{50}\text{Nb}_{50}$ system undergoes a pronounced change in properties between 1500 K and 1600 K. Fig. 1(a)-(b) show representative atomic structures obtained after 20 ns anneals. Atoms are colored by local copper concentration, \bar{c} , determined by counting the number of copper and niobium atoms in a sphere of radius 0.7 nm, centered at each atom. Concentration regions are colored on a gray color scale, with copper-rich regions ($\bar{c} > 75\%$ Cu) colored in light gray and niobium rich regions ($\bar{c} < 25\%$ Cu) colored in black. Visual inspection of a 1 nm thick, two-dimensional slice of the annealed structures at 1400 K and 1600 K reveals pronounced differences in the length scale of local composition fluctuations. At 1400 K, CMRO varies between 25 - 75% Cu with a characteristic length-scale $\lambda_c \approx 4$ nm. At 1600 K, however, $\lambda_c \approx 7$ nm, suggesting that the CMRO length-scale is approaching the simulation cell dimension. We compute λ_c as $\lambda_c \approx 2\pi / q_{MAX}$, where q_{MAX} is the wavevector at the maximum of the composition-composition Bhatia-Thornton structure factor $S_{CC}(q)$ [13]. As shown in Fig. 2(a), λ_c increases sharply when the annealing temperature exceeds 1500 K. Similar results are found in annealed $\text{Cu}_{50}\text{Nb}_{50}$ systems with different simulation cell sizes ($L_0 = 5.4$ nm and $L_0 = 12.8$ nm). The weak temperature dependence of λ_c below 1500 K shows that the atomic mobility required for diffusion and coarsening of the compositionally patterned structure is sharply reduced in the temperature range 1500-1600 K. Thus, we conclude that T_G is between 1500 K and 1600 K.

Previous simulations of the phase separating system Ni-Ag reveal the emergence of a percolating network of ISRO below T_G , in addition to stable, nanometer-scale CMRO [6]. Thus, we seek to establish whether ISRO networks might play a role in stabilizing CMRO at the glass transition. Following Luo et al. [6], we use common neighbor analysis (CNA) to probe for topological order in the $\text{Cu}_{50}\text{Nb}_{50}$ system. Consistent with the results in Ni-Ag [6], below T_G , we find a system-spanning network of atoms with fully icosahedral local packing—atoms having a 5-5-5 CNA index with 12 first nearest neighbors—centered on the smaller atom (Cu) and with neighboring atoms a mixture of Cu and Nb. A cutoff radius of 0.35 nm is used in the CNA calculation.

Following Cheng *et al.* [14], the fraction of atoms contained in either the center or vertices of icosahedra is denoted f_{ico}^{atoms} . As shown in Fig.2 (b), f_{ico}^{atoms} rises sharply at T_G . Furthermore, the spanning length L_{ico} of the largest cluster of f_{ico}^{atoms} atoms has the largest value possible in a simulation cell under periodic boundary conditions, $\sqrt{3}/2L_0$, at temperatures below T_G , demonstrating that system-spanning clusters have formed in the system [Fig. 2 (b)]. The spanning length L_{ico} is the radius of the largest sphere necessary to contain all atoms in a cluster of f_{ico}^{atoms} atoms [15].

Atoms with icosahedral order (f_{ico}^{atoms} atoms) form a continuous, percolating network below T_G and are concentrated at the interfaces between Cu and Nb-rich regions [Figs. 1(c)-(d)], clearly demonstrating a coupling between CMRO and ISRO in $\text{Cu}_{50}\text{Nb}_{50}$. In Figs. 1(c)-(d), we visualize all atoms at the CMRO interfaces ($40\% < \bar{c} < 60\%$) contained in the planar view in Figs. 1(a) and 1(b). Atoms at the CMRO interface with icosahedral order are colored red and emphasized with a 20% larger radius. Bonds between ISRO nearest neighbor atoms are colored red. At 1600 K, the CMRO interface contains only isolated icosahedra, Figs. 1(d). By contrast, at 1400 K, the icosahedra form a connected network on the CMRO interface, Figs 1(c). Distributions of icosahedra as a function of distance from interfaces $p_{ico}^{atoms}(r)$ are plotted in Figs. 1(e)-(f) and quantitatively demonstrate that ISRO order is concentrated at the CMRO interface, both below and above T_G . The total fraction of icosahedra increases by a factor of ~ 3 as

temperature decreases from 1600 K to 1400 K [Fig. 2(b)] and $p_{ico}^{atoms}(r)$ shows a clear increase in the concentration of icosahedra at the CMRO interfaces at a temperature of 1400 K [Fig. 1(c)], reflecting the visual observation in Fig. 1(c) of a connected network of icosahedra on the CMRO interfaces at 1400 K.

The presence of icosahedra at CMRO interfaces lowers the energy of the system and stabilizes CMRO against coarsening. We compute the enthalpy of formation of icosahedra, ΔH_{FORM}^{ico} , and find $\Delta H_{FORM}^{ico} = -19 \text{ kJ mol}^{-1}$. To compute ΔH_{FORM}^{ico} , for both the icosahedra network atoms and non-ISRO atoms inside Cu-rich and Nb-rich CMRO regions we find the average potential energy per atom and the average local composition. Next, we use a linear interpolation between the potential energy of the non-ISRO Cu-rich and Nb-rich region atoms to predict the average potential energy of non-ISRO atoms at the same average local composition as ISRO atoms. Finally, ΔH_{FORM}^{ico} is the difference in potential energy between the interpolated potential energy for non-ISRO atoms and the actual value computed for the ISRO atoms [Fig. S2]. Although the equilibrium state of the system is phase separated, with a positive heat of formation, the icosahedra network has a negative heat of formation with respect to CMRO interfaces, thus stabilizing the compositionally patterned structure. Coarsening would reduce the area of CMRO interfaces and therefore also the number of atoms in the icosahedra network, causing—at least initially—a net rise in energy.

Previous studies in miscible metallic glasses demonstrate that icosahedra form a mechanically stiff “elastic backbone” [16], that icosahedra are less prone to irreversible rearrangements under elastic loading than non-icosahedral atoms [17], and that the glass transition coincides with the percolation of mechanically stiff material [18]. Consistent with these findings, we find that the steady state flow stress rises abruptly below 1500 K, as shown in Fig. 2(c), demonstrating that below the glass transition there is a strain range within which $\text{Cu}_{50}\text{Nb}_{50}$ deforms elastically. The flow stress is computed under volume-conserving deformation (extension in z and equal contractions in x and y directions) at a strain rate of $\dot{\epsilon}_{zz} = 2 \times 10^9 \text{ s}^{-1}$ in strain increments of $\Delta\epsilon_{zz} = 2 \times 10^{-4}$, followed by 0.1 ps NPT ensemble MD run between each strain step. Additional simulations at strain rates as low as $\dot{\epsilon}_{zz} = 2 \times 10^7 \text{ s}^{-1}$ yield similar results

for the temperature dependence of the flow stress. We therefore test whether the icosahedra network described here is in fact a load-bearing, “elastic backbone” below the glass transition.

Below the elastic limit, the potential energy of the icosahedra network in the deformed configurations ($\dot{\epsilon}_{zz} = 2 \times 10^9 \text{ s}^{-1}$) exhibits the harmonic dependence on applied strain expected of linear elastic solids, as shown in Fig. 3. In contrast, the potential energy of atoms outside the icosahedra network is nearly strain-independent, except in the initial stages of loading, when it actually decreases due to local, irreversible relaxations. We compute these changes in potential energy with respect to a configuration at zero applied strain and identify icosahedral atoms from their strain-free CNA type. While the initial deformation is applied uniformly to the system, the MD relaxation allows all atoms to undergo independent displacements that reduce the total energy of the system. To remove thermal noise, potential energies are calculated after steepest descent potential energy minimization.

The nearly strain-independent potential energy of non-icosahedral atoms demonstrates that atoms outside the icosahedra network accommodate applied strain through liquid-like, inelastic relaxations [Fig. 3]. In contrast, the increase in potential energy with strain for the icosahedral atoms is only possible if these atoms form a connected, load-bearing network. If icosahedral clusters were disconnected and embedded in the liquid-like material, strain would be accommodated through the relaxation of the liquid-like matrix and no energy increase would occur. Destruction of icosahedra do not account for these energy changes, since f_{ico}^{atoms} changes less than 5% up to global yield and f_{ico}^{atoms} recovers completely upon unloading [Fig. S4]. Therefore, we conclude that the icosahedra network is connected and load-bearing.

The increase in potential energy of the icosahedra network in Fig. 3 is consistent with elastic deformation. However, a definitive claim of elasticity requires demonstration of reversible deformation. Similar to the procedure in [17], to demonstrate that the deformation of the icosahedra network is reversible, we deform a zero strain configuration at 1400 K (denoted *C1*) to a prescribed applied strain ϵ_{APP} at a rate of $\dot{\epsilon}_{zz} = 2 \times 10^9 \text{ s}^{-1}$ and subsequently unload the deformed configurations to 0% strain (denoted *C2*) at the same rate. The average (a)

displacement magnitude $|\Delta r|$ and (b) potential energy difference ΔPE between CI and $C2$ icosahedral atoms are computed after steepest descent potential energy minimization of each configuration, with icosahedra identified based on their type in the CI configuration. For perfectly reversible deformation, we expect both of these quantities to equal zero. The mean value and uncertainty were computed by repeating the calculation with 30 independent initial configurations at 1400 K.

As shown in Fig. 4(a) and 4(b), both $|\Delta r|$ and ΔPE for icosahedra atoms are small ($|\Delta r| < 0.03$ nm and $\Delta PE < 0.005$ eV/atom, respectively) for $\epsilon_{APP} < \epsilon_Y$ and only increase markedly after the onset of global yielding. The reversible displacements demonstrate that the deformation of the icosahedra network is elastic. The reversible changes in potential energy demonstrate that the network is mechanically stable and stiff. On the basis of Fig. 3 and Fig. 4 we therefore conclude that the icosahedra network is load-bearing, elastic, and mechanically stiff. It is responsible for the stiffening of the system below the glass transition temperature.

The presence of the load-bearing, elastic, mechanically stiff icosahedra network at the CMRO interfaces should prevent atoms from passing through it, effectively restricting diffusion to CMRO regions. Visual inspection of the CMRO region geometry suggests that the CMRO regions are system-spanning, interpenetrating ligaments. Consistent with the idea of an impermeable diffusion barrier at the CMRO interfaces that restricts diffusion to a fractal subspace, we find the diffusion exponent [Fig. 2(d)] is sharply reduced at the glass transition, with diffusion exponent $n \approx 0.5$ for temperatures between $700 \leq T \leq 1400$ K.

The Mean-Squared Displacement $r^2(t)$ (MSD) plot for a typical supercooled liquid plateaus during cage breaking, before converging to the long-time limit of Browning motion, $r^2(t) \propto t^n$ where $n = 1$ [20]. A diffusion exponent of $n < 1$ after cage breaking is therefore an indication of anomalous diffusion [19]. To compute the diffusion exponent n , we perform constant temperature and pressure ($P = 0$ GPa) NPT ensemble anneals in a 9,826 atom $\text{Cu}_{50}\text{Nb}_{50}$ system for times up to 100 ns and performed linear fits of the form $\log_{10}[r^2(t)] = n \log_{10}[t] + B$ to the measured $r^2(t)$ curves in a fitting interval of a lower and upper time [Fig. S3]. The lower

time bound is set at a time after cage breaking. Because annealing at temperatures above the glass transition yields complete phase separation after a sufficient annealing time, the upper bound time is set by a time prior to complete phase separation.

A liquid-to-solid transition due to the formation of a system-spanning, load-bearing network in a phase separating liquid mixture is the canonical description of gelation [7]. Gelation is common in colloidal [7] and polymeric systems [21]. Similar to $\text{Cu}_{50}\text{Nb}_{50}$, the percolating network that leads to gelation in some colloidal systems consists of particles packed in a preferred topology [8]. The formation of a system-spanning, load-bearing network of icosahedra along interfaces between compositionally enriched regions, coincident with the abrupt arrest of coarsening and increase in system flow stress, shows that glass transition in $\text{Cu}_{50}\text{Nb}_{50}$ may also be described as a liquid-gel transition in a phase separating metallic—rather than colloidal or polymeric—liquid.

To the best of our knowledge, gelation has not been used to describe glass transition in more conventional metallic glasses composed of compound-forming elements. Several previous findings, however, suggest that such a description may be warranted in some cases. Icosahedra have been identified as the most common form of structural short-range order in several metallic glasses [22, 23, 24] and correlated with low mobility atoms at temperatures near the glass transition [25]. Dynamic heterogeneity has been shown to couple to composition in such materials [26]. Icosahedra are the building blocks of system-spanning networks in these metallic glasses [14, 27]. Finally, we again note that icosahedra have been demonstrated to be mechanically stiff [16], that icosahedra are resistant to irreversible rearrangements under loading [17], and that glass transition has been correlated with percolation of mechanically stiff phases [18].

CMRO—albeit more compositionally complex than that in amorphous metal alloys with positive heats of mixing—has also been observed in bulk metallic glasses, such as $\text{Zr}_{41.2}\text{Ti}_{13.8}\text{Cu}_{12.5}\text{Ni}_{10}\text{Be}_{22.5}$ (Vitreloy 1) quenched at 10 K s^{-1} [28, 29]. In addition to quench rate [30, 31] and annealing time near T_G [29], the length-scale and morphology of such compositionally enriched regions are thought to reflect the proximity of T_G to a critical

temperature below which spinodal decomposition may occur [32]. Because secondary phases generally arrest shear band propagation and improve mechanical toughness [33], metallic glasses with tailored composition modulations are of technological interest. Our finding that CMRO couples with ISRO suggests that altering the ISRO network by chemical means may provide a route to controlling CMRO in these materials, thereby influencing their mechanical properties.

We thank K. J. Van Vliet for useful discussions. This material is based upon work supported by the National Science Foundation Graduate Research Fellowship under primary Grant No. 1122374. Computations were performed in part at Lawrence Livermore National Laboratory.

- 238 1. E. Ma, Progress in Materials Science **50**, 413 (2005).
- 239 2. W. L. Johnson, MRS Bulletin **24**, 42 (1999).
- 240 3. R. Banerjee *et al.*, Appl. Phys. Lett. **90**, 021904 (2007).
- 241 4. J. H. He *et al.*, Phys. Rev. Lett. **86**, 2826 (2001).
- 242 5. C. Michaelsen, C. Gente, and R. J. Bormann, J. Appl. Phys. **81**, 6024 (1997).
- 243 6. W. K. Luo *et al.*, Phys. Rev. Lett. **92**, 145502 (2004).
- 244 7. E. J Zaccarelli, Phys. Condens. Matter **19**, 323101 (2007).
- 245 8. C P. Royall *et al.*, Nature Mater. **7**, 556 (2008).
- 246 9. M. J. Demkowicz, and R. G. Hoagland Int. J. App. Mech. **1**, 421 (2009).
- 247 10. S. J. Plimpton, Comput. Phys. **117**, 1 (1995).
- 248 11. L. Zhang *et al.* Modelling Simul. Mater. Sci. Eng. **21**, accepted (2013).
- 249 12. M. P. Allen and D. J. Tildesley, Computer Simulations of Liquids (Oxford University Press,
- 250 1987).
- 251 13. A. B. Bhatia and D. E. Thornton, Phys. Rev. B **2**, 3004 (1970).
- 252 14. Y. Q. Cheng, E. Ma, and H.W. Sheng, Phys. Rev. Lett. **102**, 245501 (2009).
- 253 15. R. Zallen, The Physics of Amorphous Solids. (John Wiley and Sons, Inc., 1998).
- 254 16. A. J. Cao, Y. Q. Cheng, and E. Ma. Acta Mater. **57**, 5146 (2009).
- 255 17. F. Delogu. Intermetallics **19**, 86 (2011).
- 256 18. S. G. Mayr, Phys. Rev. B **79**, 060201 (2009).
- 257 19. D. Stauffer, Introduction to Percolation Theory (Taylor and Francis, Inc., 1995).
- 258 20. F. Faupel *et al.* Rev. Mod. Phys. **75**, 237 (2003).
- 259 21. D. Stauffer, A. Coniglio, and M. Adam, in Polymer Networks, Advances in Polymer Science,
- 260 **44**, edited by K. Dušek (Springer, 1982), 103.
- 261 22. H. W. Sheng *et al.*, Nature **439**, 419 (2006).
- 262 23. D. B. Miracle *et al.*, MRS Bulletin **32**, 629 (2007).
- 263 24. A. Hirata *et al.*, Nature Mater. **10**, 28 (2011).
- 264 25. Y. Q. Cheng, E. Ma, and H.W. Sheng. Appl. Phys. Lett. **93**, 111913 (2008).
- 265 26. T. Fujita *et al.*, Phys. Rev. B **81**, 140204 (2010).
- 266 27. J. Hwang *et al.*, Phys. Rev. Lett. **108**, 195505 (2012).
- 267 28. R. Busch *et al.*, Appl. Phys. Lett. **67**, 1544 (1995).
- 268 29. S. Schneider, P. Thiagarajan, and W. L. Johnson, Appl. Phys. Lett. **68**, 493 (1996).

- 269 30. B. J. Park, *et al.*, Appl. Phys. Lett. **85**, 6353 (2004).
270 31. C. Borchers, J. Schroers, and R. Busch, Ann. Phys. **18**, 4 (2009).
271 32. B. J. Park, *et al.*, Phys. Rev. Lett. **96**, 245503 (2006).
272 33. D. C. Hofmann, *et al.*, Proc. Natl. Acad. Sci. U.S.A. **105**, 20136 (2008).

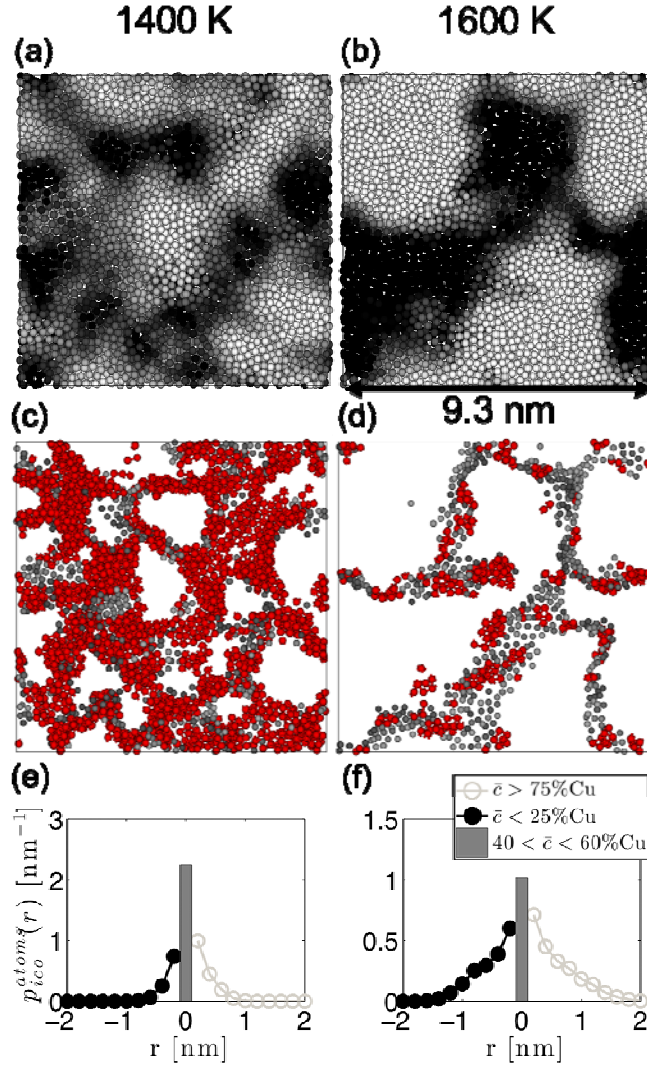


FIG 1: Visualizations of $\text{Cu}_{50}\text{Nb}_{50}$ at 1400 K (left) and 1600 K (right) after 20 ns of annealing. (a and b) A 1 nm thick slice is shown with Cu-rich regions colored light gray and Nb-rich regions colored black. (c and d) Atoms at the CMRO interface, $40 < \bar{c} < 60\% \text{Cu}$, in the slice of the top panel are visualized. Atoms participating in ISRO packing are colored red and emphasized with a 20% larger radius. Bonds between ISRO nearest neighbor atoms are colored red. (e and f) Probability $p_{ico}^{atoms}(r)$ of finding an atom in the icosahedra network at distance r from CMRO interfaces.

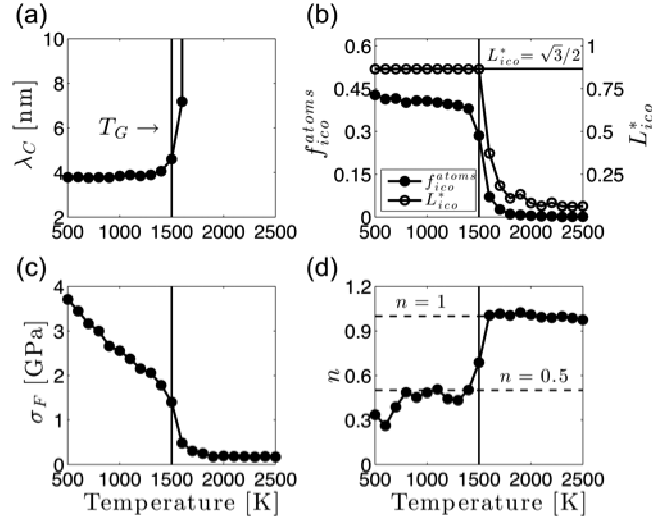


FIG 2: Temperature dependence of (a) CMRO wavelength λ_C ; (b) percent of atoms in full icosahedra f_{ico}^{atoms} and size of largest ISRO cluster divided by simulation cell edge length $L_{ico}^* = L_{ico} / L_0$; (c) flow stress σ_F ; and (d) diffusion exponent n . The vertical lines at 1500 K correspond to the glass transition temperature. All quantities computed after 20 ns annealing at indicated temperature.

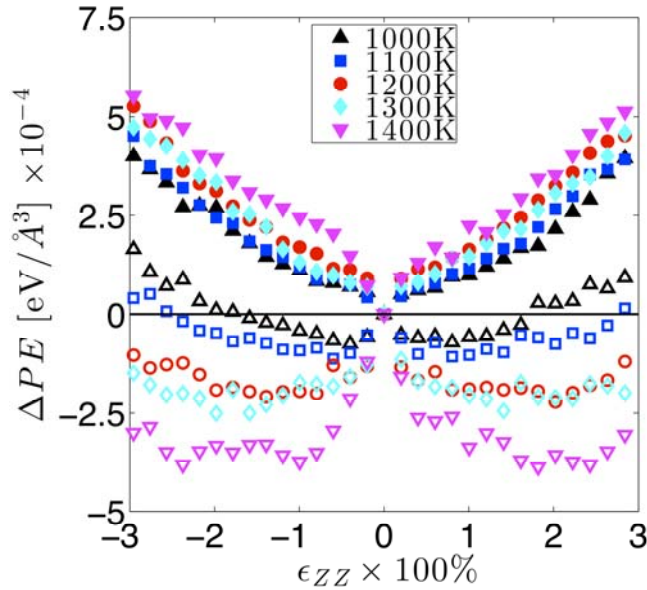


FIG 3: Change in potential energy for the icosahedra network and non-icosahedral atoms (closed and open symbols, respectively) as a function of applied strain ϵ_{ZZ} below the elastic limit.

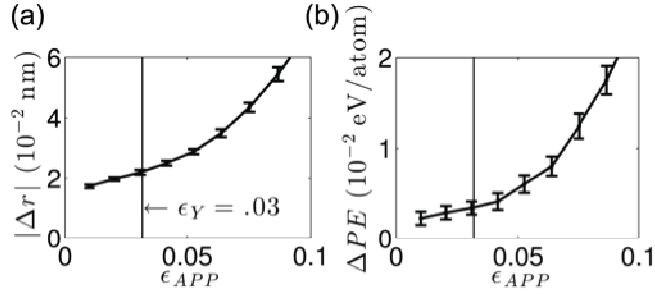


FIG 4: (a) Average displacement magnitude $|\Delta r|$ and (b) average difference in potential energy ΔPE between two zero-strain configurations, $C1$ and $C2$, as a function of applied strain ϵ_{APP} (see text for details). The vertical lines indicate the global yield strain. Error bars represent the uncertainty on the mean value, determined by averaging over 30 independent simulations.